
Article:
Lyras, KG, Hanson, B, Fairweather, M et al. (2020) A coupled level set and volume of fluid method with a re-initialisation step suitable for unstructured meshes. Journal of Computational Physics, 407. 109224. ISSN: 0021-9991

https://doi.org/10.1016/j.jcp.2019.109224

A coupled level set and volume of fluid method with a re-initialisation step suitable for unstructured meshes

Konstantinos G. Lyras[a], Bruce Hanson[a,*], Michael Fairweather[a], Peter J. Heggs[a]

[a] *School of Chemical and Process Engineering, University of Leeds, Leeds LS2 9JT, United Kingdom*

Abstract

This paper presents a coupling method of the level set and volume of fluid methods based on a simple local-gradient based re-initialisation approach that evaluates the distance function depending on the computational cell location. If a cell belongs to the interface, the signed distance is updated based on a search in the neighbouring cells and an interpolation procedure is applied depending on the local curvature or the sign of the level set function following [D. Hartmann, M. Meinke, W. Schröder, Differential equation based constrained reinitialisation method for level set methods, J. Comput. Phys. 227 (2008) 6821-6845]. The search algorithm does not distinguish between the upwind and downwind directions and hence it is able to be used for cells with an arbitrary number of faces increasing the robustness of the method. The coupling with the volume of fluid method is achieved by mapping the volume fraction field which is advected from the isoface evolution at a subgrid level. Consequently, the coupling with the level set approach is utilised without solving the level set equation. This coupled method provides better accuracy than the volume of fluid method alone and is capable of capturing sharp interfaces in all the classical numerical tests that are presented here.

Keywords: level set, volume of fluid, re-initialisation

*Corresponding author
Email address: b.c.hanson@leeds.ac.uk (Bruce Hanson)

1. Introduction

1.1. Scope

In implicit methods for calculating the interface between two fluids flowing in a fixed mesh, the interface is captured using a scalar field advected in space. The scalar field (marker) has to be intrinsically connected to the absence or presence of the liquid phase. These methods are easily extended into three-dimensions but might require fine meshes to resolve the interface. The same limitation holds for front-tracking methods. Here, we are interested in interfaces for multiphase flows such as bubbles, droplets, and jets for liquid/liquid and liquid/gas interactions. The most commonly cited implicit methods are the volume of fluid method (VOF [1–11] and the level set (LS) methods [12–20]. The level set formulation is utilised by transporting a continuous function, as in the VOF method. The level set method has been developed for an accurate representation of complex interface and boundaries for a wide range of applications including among others the areas of shape optimisation [21], computer graphics [22], medical imaging [23], grid generation [24], seismology [25], and superconductors [26]. For fluid interfaces, and particularly in the two-phase flows considered in this paper, the interface of the fluid is defined by the zero-level of a signed distance function and the level set method provides an accurate representation of the curvature of the interface. One common characteristic of this method and VOF is that the user does not need to modify the method regardless of the complexity of the geometry since both VOF and level set adjust naturally to any topological changes. One of the main differences between the two methods, is the transition from one fluid to the other, which in the level set method occurs gradually rather than as in the volume of fluid approach where the interface exists in a one-cell layer in between the two fluids.

Despite its efficiency in calculating the interface, the level set method has the shortcoming that mass conservation is not guaranteed. This barrier can be overcome by coupling the method with the volume of fluid approach which is conservative, with the level set being highly accurate. This idea was im-

plemented first by Bourlioux [27] and Sussman and Puckett [28] giving a new method, the coupled-level-set-volume-of-fluid (CLSVOF) approach. Use of the CLSVOF showed that advecting both the volume fraction and distance functions can conserve mass increasing the accuracy of VOF, and providing the basis for different variations of the level set method which have been used in chemical process, aerospace and automotive industries.

The coupling of these two approaches does, however pose challenges for the interface reconstruction and the re-initialisation procedures that have to be addressed to successfully simulate fluid flows in the case of three-dimensions or non-orthogonal meshes. In [29] a piecewise-linear interface construction/calculation (PLIC) method is described for advecting the interface, with the level set function used to calculate the curvature. The volume of fluid in a computational cell defines a plane, which is constructed by the intersection points with the cell. The signed distance function is taken as the minimum distance from a finite volume centre to an interface-plane that is defined by a stencil of cells. This VOF-PLIC approach was developed for unstructured meshes in both two and three-dimensions. A similar approach was employed in [30] where the LS-VOF coupling evaluated the level set function from the minimum distance from an arbitrary cell centroid to the zero-level. In addition, no special re-initialisation process was employed, following the geometric operation proposed in [31] (the so-called coupled volume of fluid and level set, a.k.a. VOSET, method) to calculate the level set function near the interface. The VOSET method can be applied to accurately compute the curvature and smooth discontinuous physical quantities near the interface for both structured and unstructured meshes. A different LS-VOF coupling suitable for overlapping and moving structured grids was proposed in [32] using a PLIC method for the advection of the volume of fluid approach. The interface was advected using a hybrid split, Eulerian implicit-Lagrangian explicit interface advection scheme which provided good results for the classical test of a deforming three-dimensional sphere. In [33] the idea of flux polygon reconstruction using vertex velocities was employed to evaluate the VOF function. The computed volume fraction was then corrected

by a flux corrector estimated using the face velocities. The level set function was advected by a high order total variation diminishing (TVD) scheme and then re-initialised in a narrow band around the interface with a geometric procedure. In [34] the idea of the area of fluid was employed for advecting the volume fraction developing an iterative clipping and capping algorithm for the coupling of the level set and volume of fluid methods. Both the LS and VOF functions are advected by solving a transport equation for each one of them: the volume of fluid is advected employing an interface compression scheme whereas the LS function uses a van Leer TVD scheme. Despite its efficiency in calculating the interface, the LS method has the shortcoming that mass conservation is not guaranteed. This barrier can be overcome by coupling the method with VOF approach which is conservative, and the LS which is highly accurate (see [27] and [28]). In [35] a conservative LS method was developed, which has been demonstrated to conserve mass. This has been the basis of different variations of the LS method which have been used in multiphase flows [34, 36–38]. Coupling the volume of fluid with level set it is possible to combine the benefits of both methods providing an improvement in capturing of the sharp interface with a reasonable accuracy for mass conservation. The ultimate purpose of the correct advection of the level set is the accurate calculation of curvature and mixture properties, in line with the one-fluid approach.

1.2. Objectives

This paper presents a novel coupled LS and VOF method capable of simulating the interface of two fluids, of different properties. The first part of the method is the re-initialisation step of the signed distance function. All traditional level set methods face the problem of finding the proper values of the signed distance function, ψ, which satisfy the Eikonal equation, $|\nabla\psi| = 1$. This is usually done by solving the level set equation with a high order approach in time and space to minimise the error, and re-initialising the distance function to avoid the displacement of its initial value ψ_0 [39]. In this paper a partial differential equation re-initialisation method is presented based on the works of

Russo and Smereka [40] and Hartmann et al. [41] which allows the simple and efficient calculation of the distance function across the interface. The presented formulation is second-order in space and constructed for computational cells of arbitrary shape, and is tested for both structured and unstructured meshes. The initial value of the distance function ψ_0 in the coupled volume of fluid and level set methods is derived by advecting the volume fraction with either an algebraic or a geometric method. The VOF method for the research presented here, considers the motion of an isoface in a computational cell and advecting it, using the isoAdvector method proposed in [42] and implemented in the open source CFD code OpenFOAM [43]. The isoface is properly advected within a time step, estimating the volume transport across a face before moving on to the next time-step solution. The complete volume fraction advection algorithm is described in detail in the following sections. The coupling of the LS and VOF methods is developed here within OpenFOAM and is done without the need to solve the LS function equation. The approach maps the volume fraction to ψ_0 directly from the VOF step, and then corrects the signed distance function. In order to preserve its distance function character, the level set function is re-initialised in two parts. First, the distance function is calculated for the cells at the interface and is mapped to the level set function. In the second part the re-initialisation equation is solved for the cells adjacent to the cells at the interface [39, 41]. Comparisons of the VOF and the coupled LS-VOF for classical numerical tests reveal that the LS step improves the accuracy of solution and boosts the ability of the method to capture sharp interfaces.

2. Motivation and methodology

2.1. Level set method

The interface which separates the two fluids is represented by the level set function $\psi(\mathbf{x}, t)$. Depending on whether a given point $(\mathbf{x}, t)$ with a normal distance to the interface d, exists in one fluid or the other, $\psi(\mathbf{x}, t)$ is defined as

$\psi(\mathbf{x}, t) = +d$, or $\psi(\mathbf{x}, t) = -d$, respectively. The interface Γ is then defined as the set of points that belong to the zero-level, as follows

$$\Gamma = \{\mathbf{x} | \psi(\mathbf{x}, t) = 0\} \tag{1}$$

The level set function is then a distance function that is defined wherever an interface exists. The distance function can be advected using

$$\frac{\partial \psi}{\partial t} + \mathbf{u} \cdot \nabla \psi = 0 \tag{2}$$

where $\mathbf{u}$ is the velocity field. The above equation can be solved using any high order scheme for hyperbolic systems of the ENO (essentially non-oscillatory) schemes family or the Runge-Kutta method [44]. A similar advection equation is used for the marker function in volume of fluid methods. Adding extra algebraic terms to the right-hand side of this advection term, compresses the interface, leading to conservative forms of both methods [35, 45].

2.2. Re-initialisation step

Although the distance function is advected well for $\psi = 0$, it tends to fail to remain an actual distance function when solving Eq. (2) because of the very small or large values the magnitude of the gradients $|\nabla \psi|$ might attain on either side of the interface compromising accuracy [46]. Consequently, a re-initialisation step is required for the ψ-equation [39]. This is an extra step to straighten the distorted shape of the function ψ, which might be caused by the numerical solution of the convection equation or by the complicated fluid velocity fields. With the re-initialisation step the LS function and the shape of the interface can be preserved as much as possible throughout the simulation. This is achieved by solving the following Eikonal equation [15]

$$\frac{\partial \psi_d}{\partial \tau} = \mathrm{sgn}(\psi)(1 - |\nabla \psi_d|) \tag{3}$$

where $sgn()$ is the sign function. The new corrected distance function, ψ_d, is calculated iteratively knowing ψ which is used as an initial guess in the re-initialisation process, $\psi_d(t = 0) = \psi$. In Eq. (3), τ is a fictitious time-step

which can be associated to the grid resolution. Previous studies suggest various values for τ (see [36, 41]) and $\tau = 0.1\Delta x$ is considered in this study. The re-initialisation equation can be solved in steady state and ideally converges to $|\nabla\psi_d| = 1$. Previous numerical works have addressed the re-initialisation problem providing algorithms for either structured [40, 41, 47] or unstructured computational meshes [48]. In this study, we choose to incorporate and employ for unstructured meshes the algorithm of [41], which is a partial differential equation based localised method, which imposes the zero-displacement constraint on the zero LS. If d_P is the desired signed distance function at the interface for cell P, then d_P is the value of ψ that has to be used to properly advect the LS function. An initial guess, $\tilde{d}_P$ of the distance is required during the re-initialisation step. In [40] a central difference scheme was suggested based upon the knowledge of the upwind or downwind cells of cell P. However, in [41] a modified expression for $\tilde{d}_P$ was utilised by imposing additional conditions that depend on how the LS changes along the three co-ordinate directions x, y and z. In this present study, the distance function is calculated first for the cells at the interface and is then used to update the level set function. This is done using first order expressions as proposed in [40]. The Eikonal equation for ψ is then solved in a narrow band of cells adjacent to the cells that belong to the interface [41]. The algorithm starts by searching for all the cells at the interface Γ of the two fluids and performing the re-initialisation step. The algorithm is as follows:
Step 1: For all cells P at the interface Γ, the signed distance function $\tilde{d}_P$ is estimated first using the values of the level set function before the re-initialisation, denoted for cell P by $\tilde{\psi}_P$. It can be written that

$$\tilde{d}_P = \tilde{\psi}_P / \left[\sum_{\zeta} (\partial_\zeta \tilde{\psi}_\zeta)^2 \right]^{1/2} \tag{4}$$

,where $\partial_\zeta \tilde{\psi}_\zeta$ is the discrete derivative in the ζ direction [47]. The maximum between the central and upwind differences can be used for calculating the derivatives in this expression [40]. In the present study, upwind differences are considered, employing some of the neighbouring cells. First, a search is

performed for all the faces f of the cell P and if a neighbouring cell N that shares f with P also belongs in Γ, the discrete derivative of $\tilde{\psi}_P$, $\partial_f \tilde{\psi}_P$, is calculated as:

$$\partial_f \tilde{\psi}_P = \frac{\tilde{\psi}_P - \tilde{\psi}_N}{x_P - x_N} \tag{5}$$

Let the number of all these $\Gamma-$neighbours be $N_{P,\Gamma}$. Then we use $N_{P,\Gamma}$ discrete derivatives. In the case of both upwind ($\tilde{\psi}_{i-1}$) and downwind ($\tilde{\psi}_{i+1}$) cells belonging to the set Γ, then both differences are considered in the expression for $\tilde{d}_P$. Since, $2[(\partial_{i-1}\tilde{\psi}_{i-1})^2 + (\partial_{i+1}\tilde{\psi}_{i+1})^2] \geq [(\tilde{\psi}_{i+1} - \tilde{\psi}_{i-1})/\Delta x]^2$, and given the fact that we cannot have more than $\lfloor N_{P,\Gamma}/2 \rfloor$ pairs of such central differences, the sum of all these central differences for cell P in x, y, z (the right part of the above inequality) will be no greater than the quantity in the denominator of the signed distance function $\tilde{d}_P$ in Eq.(4), considering all the $N_{P,\Gamma}$ faces e.g. $N_{P,\Gamma}\left[\sum_f (\partial_f \tilde{\psi}_f)^2\right]^{1/2}$. For the tests presented here, we use this expression for calculating $\tilde{d}_P$. We use these $N_{P,\Gamma}$ derivatives to calculate the target value of the LS which can be written as:

$$\tilde{d}_P = \frac{\tilde{\psi}_P}{(N_{P,\Gamma} \sum_{k=1}^{N_{P,\Gamma}} (\partial_{f_k} \tilde{\psi}_{f_k})^2)^{1/2}} \tag{6}$$

Note that the summation in Eq.(6) is performed through the cell faces and thus $N_{P,\Gamma}$ is less than or equal to the number of faces of the cell P. The above expression for $\tilde{d}_P$ is bounded by the special case of a three-dimensional structured mesh introduced in [41] for Cartesian meshes with pre-defined directions, x,y,z. The upwind discretisation was employed in [41, 47] and was proven capable of avoiding any oscillations at the interface that could be caused by central differences.

Step 2: The following step is performed for all the cells in Γ that have negative curvature κ (calculated from the interface normal $\mathbf{n}$, $\kappa = \nabla \cdot \mathbf{n}$) or satisfy the condition $\kappa = 0$ and $\tilde{\psi} \leq 0$, (following [41]). A search is considered for all the neighbouring cells that share the same face f_k with cell P that have an opposite sign for ψ_P (for instance, the neighbours N_1, N_2 in Fig.1). Let

the number of these cells be M_P, then, the signed distance function and LS functions $d_P, \tilde{\psi}_P$ for the cell-centre P are interpolated with the same second-order operator as in [41] as:

$$(d)_p = \frac{1}{M_P}\sum_{k=1}^{M_P} d_{f_k}$$
$$(\tilde{\psi})_p = \frac{1}{M_P}\sum_{k=1}^{M_P} \tilde{\psi}_{f_k} \tag{7}$$

Assuming that the ratio of the LS function with its interpolated value remains the same as the ratio of the signed distance value with its interpolated value, the position of the zero-level is fixed (a constraint imposed in [41]). The target value of the LS function is then calculated as [41, 47]

$$d_P = \tilde{\psi}_P \frac{\sum_{k=1}^{M_P} d_{f_k}}{\sum_{k=1}^{M_P} \tilde{\psi}_{f_k}} \tag{8}$$

where the summation in Eq.(8) is performed over all the M_k cells that are neighbours of the cell P, at a face f_k with a corresponding d_{f_k}, such that $\psi_P \psi_{f_k} \leq 0$ (ψ_{f_k} is calculated at the cell centre of the neighbouring cell).

Step 3: The LS function for cell P is updated at the interface according to $\psi_P = d_P$, as suggested by [41].

Step 4: The re-initialisation equation is solved for the rest of the cells adjacent to the interface Γ but with a marker function value equal to 0 or 1 (see Fig.2). Eq. (3) is then solved in steady state:

$$\psi^{n+1} = \psi^n - \Delta\tau S(\tilde{\psi})(|\nabla\psi| - 1) \tag{9}$$

where $S(\tilde{\psi}) = \tilde{\psi}/\sqrt{\tilde{\psi}^2 + |\nabla\tilde{\psi}|^2\Delta x^2}$ is a modification of the sign function and Δx is the cell size. The gradient magnitude is $|\nabla\psi| \cong H_G(D_\zeta^- \psi^n, D_\zeta^+ \psi^n)$ is the Godunov-Hamiltonian of the LS function from the previous iteration through all faces of the particular cell. Here, the terms $D_\zeta^- \psi^n, D_\zeta^+ \psi^n$ are the first order approximations of the gradient of ψ along the $\zeta-$direction, $\zeta = x, y$ or z

depending on whether the upwind "-" or the downwind cell is considered "+"

$$D_\zeta^- \psi^n = \frac{\psi_i^n - \psi_{i-1}^n}{\Delta\zeta}, \qquad D_\zeta^+ \psi^n = \frac{\psi_{i+1}^n - \psi_i^n}{\Delta\zeta} \tag{10}$$

The need to use first order terms arises from the large gradients across the interface that require an accurate and stable method of calculating H_G. The above formulation is the basis for various fast marching algorithms with structured meshes, e.g. [15, 28, 41]. Here, the normal gradient of the level set function $\nabla_f^\perp$ is calculated for all the faces f based on the orientation of the normal at the face. In general

$$\nabla_f^\perp = \alpha_{corr}(\psi_P - \psi_n)/|\Delta\zeta|\hat{\zeta} + (\hat{\zeta} - \alpha_{corr}\Delta\zeta)\nabla(\psi)_f \tag{11}$$

where α_{corr} is the inverse cosine of the angle between the cell centres and the normal face, and $\nabla(\psi)_f$ is the linearly interpolated gradient at the face f. This expression is used for meshes that non-orthogonality is high, and for orthogonal meshes the second part of the right-hand-side is omitted. Following [34] in the case of unstructured meshes, one possible approach is to select the upwind cell from all face-neighbouring cells of the central cell P as the one whose centre position is closest to the line through the centre and downwind nodes. If the position vector is $\mathbf{\Delta}\zeta$ and the unit vector is denoted as $\hat{\zeta}$, then if $\psi < 0$ and $\mathbf{\Delta}\zeta \cdot \hat{\zeta} < 0$ or $\psi > 0$ and $\mathbf{\Delta}\zeta \cdot \hat{\zeta} > 0$ we have:

$$a_\zeta = min\left(\nabla_f^\perp \psi \cdot \hat{\zeta}\right) \tag{12}$$

If $\psi < 0$ and $\mathbf{\Delta}\zeta \cdot \hat{\zeta} > 0$ or $\psi > 0$ and $\mathbf{\Delta}\zeta \cdot \hat{\zeta} < 0$ then:

$$a_\zeta = max\left(\nabla_f^\perp \psi \cdot \hat{\zeta}\right) \tag{13}$$

The Hamiltonian-Godunov term is simply calculated as

$$H_G = \sqrt{max(a_x^2) + max(a_y^2) + max(a_z^2)} \tag{14}$$

For the test cases presented here, no significant difference was observed using an explicit calculation of the gradient of ψ in Eq. (9). This can be performed for

unstructured meshes for a cell P with volume $V^{(P)}$, faces f and surface vector $\mathbf{S_f}$ using:

$$\nabla\psi_d^{(P)} = \frac{1}{V^{(P)}}\sum_f \psi_f \mathbf{S_f} \tag{15}$$

The steady solutions of Eq. (9) are distance functions. Furthermore, since $\mathrm{sgn}(0) = 0$, then $\psi_d(\mathbf{x}, \tau)$ has the same zero-level as ψ.

The fictitious time step for the steady state iterations $\Delta\tau$, has to be chosen so that an accurate value of the LS function is obtained within a reasonable number of iterations. $\Delta\tau$ can be a fraction of or equal to the mesh size, Δx [34, 40]. For the simulations performed in this study, $\Delta\tau = 0.1(\Delta x\Delta y\Delta z)^{\frac{1}{3}}$ has been chosen.

A fixed small number of iterations is needed in practice to guarantee the distance function property near the interface. Following [46], the number of iterations depends on the thickness of the interface $2\epsilon\Delta x$, with ϵ being the layer of cells across which the re-initialisation step takes place (the correction is kept local). The iteration process can stop after 2ϵ time-steps, and a value of $\epsilon = 1.5$ is chosen here so that the interface is spread over a thickness of three cells (see also Step 4). Finally, for both formulations, Eq.(3) and Eq.(9), the initial value $\psi_0(\mathbf{x}) = \psi(\mathbf{x}, 0)$ can be taken from the volume fraction α assuming the interface position is at the iso-surface contour α-0.5, (as in [49]) and is written as a function of the cell size [36].

2.3. Utilising the one-fluid approach

Having calculated the LS function, the mixture properties such as density and viscosity can be evaluated with the one-fluid approach. The two fluids are treated as one fluid with properties that change across the interface [7]. To achieve numerical robustness, a smeared Heaviside function, H, is used [35] defined as

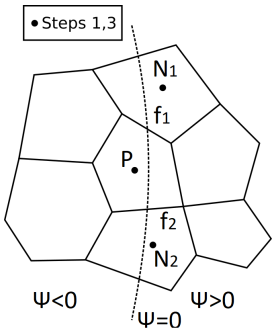

Figure 1: Steps 1-4 performed for a computational cell P in a non-uniform two-dimensional mesh.

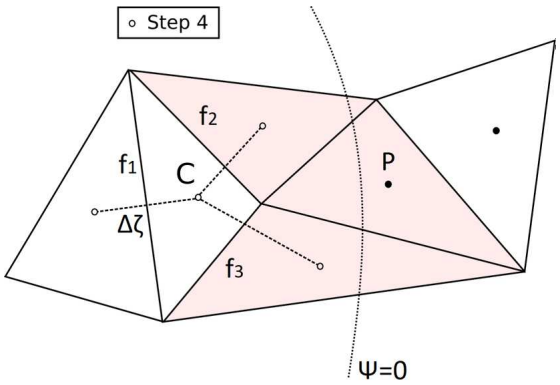

Figure 2: Steps 4 performed for a computational cell C that does not belong to Γ.

$$H(\psi) = \begin{cases} 0 & \text{if } \psi < -\epsilon \\ \frac{1}{2}\left[1 + \frac{\psi}{\epsilon} + \frac{1}{\pi} sin(\frac{\pi\psi}{\epsilon})\right] & \text{if } |\psi| \leq \epsilon \\ 1 & \text{if } \psi > \epsilon \end{cases} \tag{16}$$

294 The pseudo-fluid properties can be then calculated as

$$\rho = \rho_1 H + \rho_2(1 - H) \tag{17}$$

$$\mu = \mu_1 H + \mu_2(1 - H) \tag{18}$$

295 The surface tension force acting on the interface is calculated as [36, 50]

$$F_\sigma = \sigma\kappa\delta(\psi)\nabla\psi \tag{19}$$

Here $\delta()$ is the Dirac function which is employed for limiting the effect of the surface tension force in the vicinity of the interface, a region with thickness ϵ

$$\delta(\psi) = \begin{cases} 0 & \text{if } |\psi| > \epsilon \\ \frac{1}{2\epsilon}\left[1 + cos\left(\frac{\pi\psi}{\epsilon}\right)\right] & \text{if } |\psi| \leq \epsilon \end{cases} \tag{20}$$

The curvature and the gradient can be discretised (since ψ is a continuous function) and the surface tension can be calculated at the cell faces using

$$F_\sigma = (\sigma\kappa)_f \, \delta_f(\psi)\nabla_f^\perp\psi \tag{21}$$

2.4. Numerical formulation of coupling Volume of fluid and level set methods

The initial value ψ_0 used in Eq. 3 is the starting point for the re-initialisation iterations and the link with the VOF method. A straightforward approach without solving the LS equation [36, 49] is to use

$$\psi_0 = (2\alpha - 1)\tilde{\Delta}x \tag{22}$$

In the above initial value the $\alpha-0.5$ iso-surface is used as a starting point for the signed distance function. The percentage of the interface thickness, $\tilde{\Delta}x$ here equal to $0.8\Delta x$, is introduced for numerical robustness and gives a ψ_0 value within $(-\epsilon, \epsilon)$ for the cells belonging to Γ. The volume fraction α can be advected with various methods [46, 51–53]. The advection of the volume fraction depends on the normal to the interface, usually performed employing values in the neighbouring cells by selecting the orientation of the interface. The coupling methods used with the VOF approach in [34, 36] use a transport equation for the volume fraction with the MULES limiter. Even with the addition of an extra term for compressing the interface, $\alpha(1-\alpha)U_r$, where U_r is the relative velocity between the two fluids [45], the interface might still diffuse as previously

shown in numerical tests in [30, 42], which can be limited, coupling this scheme with a level set method [34].

The approach in [42] is used to advect the volume and the surface submerged in one fluid inside each cell at the interface. The idea is that after every time-step, the iso-surface inside a computational cell (at Γ) splits the cell C with volume V_C into two different parts: one occupied by fluid 1 with volume fraction α and the other one filled with fluid 2 with volume fraction $(1-\alpha)$. Let $X_1, X_2, ..., X_k$ be the nodes of a cell at the interface, as in Fig.3. The sub-grid face defined from the line connecting all the intersection points x_m of the iso-surface and the cell edges, the isoface, is assumed to be advected with a velocity equal to the velocity of the previous time step and is calculated by solving the momentum equation. The points x_m at a cell edge $(X_k X_l)$ can be evaluated from

$$x_m = X_k + \lambda_\alpha (X_l - X_k) \tag{23}$$

where λ_α is a weight function defined by interpolating at each node X_i the volume fraction of the surrounding cells. Hence, $\lambda_\alpha = (\alpha - \alpha_k)/(\alpha_l - \alpha_k)$, where α_k, α_l are the corresponding values at the nodes X_k, X_l. With this linear interpolation the isoface will split the cell into one subcell of fluid 1 with volume $\Delta V_C(\alpha)$ and another one with volume $V_C - \Delta V_C$ of fluid 2. The isoAdvector method of Roenby et al. [42] is then performed to find the optimum isovalue a^* such that $\alpha = \Delta V_C(\alpha^*)/V_C$. A proper value of α^* will cut the cell C into two subcells with volumetric proportions calculated from the previous guess of the volume fraction α_C leading to a more accurate reconstruction of the interface than would be obtained using the 0.5-isovalue. The procedure resembles the re-initialisation step in the correction of the LS method. Using a third degree polynomial $p_\alpha(x)$ for interpolating the isovalue, we have the following

constraints:

$$\begin{aligned} p_\alpha(x_k) &= f_k \\ p_\alpha(x_k + \frac{x_k - x_l}{3}) &= \frac{f_k}{3} \\ p_\alpha(x_k + \frac{2(x_k - x_l)}{3}) &= \frac{2f_k}{3} \\ p_\alpha(x_l) &= f_l \end{aligned} \tag{24}$$

Finding the polynomial that passes though these points, can then be used to calculate the isovalue and the isoface which are now defined since both the vertices and its area, E_m, are known.

Next step, is the time evolution of the isoface within a cell. The isoface will have a centre x_c and velocity $\mathbf{u_c}$ with a normal vector $\mathbf{n_c}$, as in Fig.3. The isoface will then pass all the vertices X_k at time t_k which is calculated in [42] from

$$t_k = t + \mathbf{dx_i} \cdot \frac{\mathbf{n_c}}{\mathbf{u_c}} \tag{25}$$

where the vector $\mathbf{dx_k}$ connects the isoface centre with the vertices, $\mathbf{dx_k} = X_k - x_c$. Knowing the time t_k allows calculation of the face-interface line during the solution time step δt. The submerged area can be integrated using all the time integrals $[t_k, t_{k+1}]$ such that $t < t_k, t_{k+1} < t + \delta t$. If there are N_{sub} such time steps then:

$$\int_t^{t+\delta t} E_m d\tau' = \sum_{k=1}^{N_{sub}} \int_{t_k}^{t_{k+1}} E_m d\tau' \tag{26}$$

The volume of the fluid with the isoface E_m is easily calculated, since:

$$\Delta V_f^n = \frac{\phi_f}{|\mathbf{S_f}|} \sum_{k=1}^{N_{sub}} \int_{t_k}^{t_{k+1}} E_m d\tau' \tag{27}$$

using the volumetric fluxes and the face area at face f, ϕ_f and $|\mathbf{S_f}|$. The volume fraction is then updated explicitly using the transported volume at each face as

$$\alpha^{t+\delta t} = \alpha^t - \frac{1}{V_C} \sum_{f=1}^{N_f} \Delta V_f^n \tag{28}$$

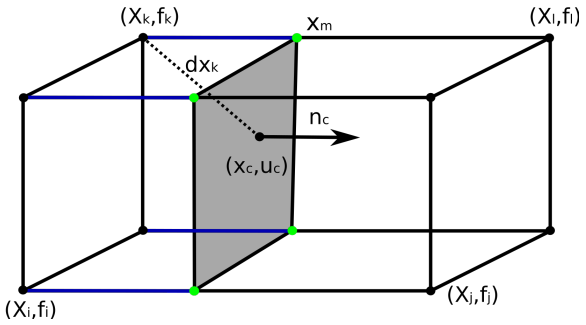

Figure 3: Isoface advection step inside a computational cell. Isoface nodes within the interval $[t_k, t_{k+1}]$ (green points), isoface (shaded face) and face-interface lines (blue).

The coupling algorithm of this isoface-level-set-volume-of-fluid (ILSVOF) method can be described in the following main steps. The numerical fields are initialised together with the LS function. The dynamic pressure is used to avoid any sudden changes in the pressure at the boundaries for hydrostatic problems. The time loop starts by correcting the interface and the volume fraction at the boundaries. The volume fraction is advected, and corrected, and new values of α are assigned at the boundaries. The new LS function ψ_0 is calculated using the results of the advection equation. Next, ψ is re-initialised applying Steps 1-4 described for the re-initialisation procedure, to obtain the signed distance function, and the interface at the boundaries is corrected. The new interface curvature is calculated. The mixture properties and fluxes are updated using the LS function. For instance, for density $\rho = \rho_1 H + \rho_2(1 - H)$ is used, where $H()$ is a Heavyside function of ψ which is used instead of ψ for numerical purposes in LS methods, [35]. The Navier-Stokes equations are solved for velocity and pressure using the pressure implicit with splitting of operators (PISO) method. The process starts again, by first correcting the interface and the volume fraction at the boundaries and then, following the described steps after that.

3. Numerical tests and discussions

The performance of the proposed numerical methodology is tested using simple test problems involving two fluids of different densities and viscosities. The problems, in both two and three-dimensions, include comparisons between the presented method and other numerical works with or without the level set implementation. Different indicators are used for monitoring the method's performance in terms of shape conservation and boundedness. The numerical tests presented here concern both structured and unstructured meshes and different mesh resolutions are examined for the presented test cases.

3.1. Two-dimensional rotating disc

The rotating disc has been proposed in [54] and considers a disc that undergoes a significant interface deformation and is used here to evaluate the ability of the presented methodology to transport under-resolved interface structures [6, 9, 33, 55]. The computational domain is a unit square which contains a disc with radius R placed in the domain so that the disc centre is at $(x, y) = (0.5, 0.75)$. The rest of the domain is filled with a fluid of lower viscosity than the one of the disc. The velocity field is given by

$$u(x, y, t) = -sin^2(\pi x)sin(2\pi y)cos\left(\frac{\pi t}{T}\right) \tag{29}$$

$$v(x, y, t) = sin(2\pi x)sin^2(\pi y)cos\left(\frac{\pi t}{T}\right) \tag{30}$$

The velocity field changes in time and space and causes the disc to rotate so that the initially circular disc is stretched with time (the flow lasts for one period T). The resulting filament will then stretch until $t = T/2$ at which point the velocity field reduces to its minimum and becomes zero, according to Eq. (29). For the simulations here, a period of $T = 8$ was used with a total simulation time of $8s$. The physical parameters considered are summarised in Table 1. Two different types of mesh have been used, quadrilateral and triangular, as the ones shown in Fig. 4 each using a coarse, medium and a fine meshes respectively. The

results for the new method are shown in Tables 2 and 3. A comparison of the ILSVOF methodology described here, with the case of using only the VOF method [42] without the level set, is also included. Previous studies in [42] have shown that the volume of fluid method of [42] provides higher accuracy for interface advection than the volume of fluid approach of [45] based on, hence only the error in shape preservation reported in [42] is included for comparisons in Tables 2 and 3. Some results obtained using only [45] approach for two and three-dimensional cases are presented for qualitative comparisons in Fig. 5. The error

$$E_\alpha = \frac{\sum_i V_i |\alpha_i - \alpha_{exact}|}{\sum_i V_i \alpha_{exact}} \tag{31}$$

is used as a quantitative measure of the shape preservation. Here, the exact solution is defined as the initial position of the rotating disk and E_α is calculated over all cells of the domain. The extent to which the solution stays within the range of physical values is also tested, considering the minimum and maximum of the liquid volume fraction of the rotating disc, $\min(\alpha)$ and $\max(\alpha)$ respectively, also calculated over all cells of the domain. One should expect ideally to have $0 \leq \alpha \leq 1$ for all cells.

Table 1: Physical properties for rotating disc simulations.

	Physical and numerical parameters
Heavy fluid density	1110 kg/m^3
Light fluid density	806 kg/m^3
Heavy fluid kinematic viscosity	1.017e-06 m^2/s
Light fluid kinematic viscosity	2.35e-06 m^2/s
Length of square domain	1 m
Period T	8 s
CFL number	0.3

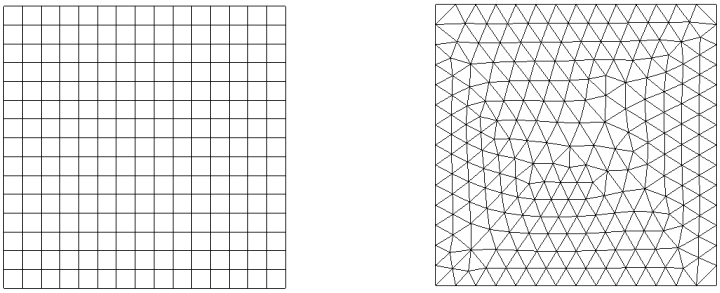

(a) Quadrilateral mesh. (b) Triangular mesh.

Figure 4: Meshes used to discretise the domain used (coarse mesh study).

As indicated in the results of Fig. 5, increasing the mesh resolution, increases the sharpness of both methods with E_α decreasing. The mesh resolution is a important parameter that influences the ability of the interface capturing method to resolve the ligament stretching. The sharp tail at the end of the deforming ligament fails to be resolved at the subgrid scale. In all cases, at the time of maximum stretching, $t = T/2$, the rotating spiral thickness becomes equivalent to the local cell size and fragmentation starts to be noticeable (Fig. 5). The observed volume sharpness error was generally of the same order as that obtained from the other approaches, or smaller. The same behaviour is observed in boundedness were the marker function, α, stays above the minimum value of 0 and below or equal to 1, contrary to the solution obtained without the level set step. The ILSVOF method maintains similar trends for the error measures for both structured and unstructured meshes (Table 3). A comparison between the presented ILSVOF and the VOF methods is shown for $t = T/2$ in Fig. 6 for the case of the medium size quadrilateral meshes using the OpenFOAM VOF methods of [42] and [45] which employs the multidimensional universal limiter with explicit solution (MULES) scheme [56]. As the rotating vortex thickness becomes progressively smaller, the droplets pinch off and the local interface curvature becomes of the same order as the mesh size. The decreasing interface curvature causes the isoface, used here to advect α, to become less accurate for

the resulting droplet motion. The coupling with level set shows that it is possible to have less diffusion at the tip for the rotating filament for both quadrilateral and triangular meshes (Fig. 7). The gradients appearing during the deformation of the vortex might have an effect on shape preservation, via Eq. (6), even though the vortex reverses after $t = T/2$ back to its initial position, but these do not seem to reduce the solution accuracy, at least for the re-initialisation steps used here which usually varied from 2 to 5. The ILSVOF retains the vortex shape better than the other methods at the maximum stretching position. Using the interface compression scheme MULES, sharpness can also be maintained at $t = T/2$, but this interface compression might cause the rotating spiral to break-up, fragmenting the vortex in the interval $[T/2, T]$ which is more evident at $t = T$ in Fig. 6 and Fig. 7. The increased error in the averaged volume fraction for this approach is also reported in previous studies in [34], and is observed here in both structured and unstructured methods.

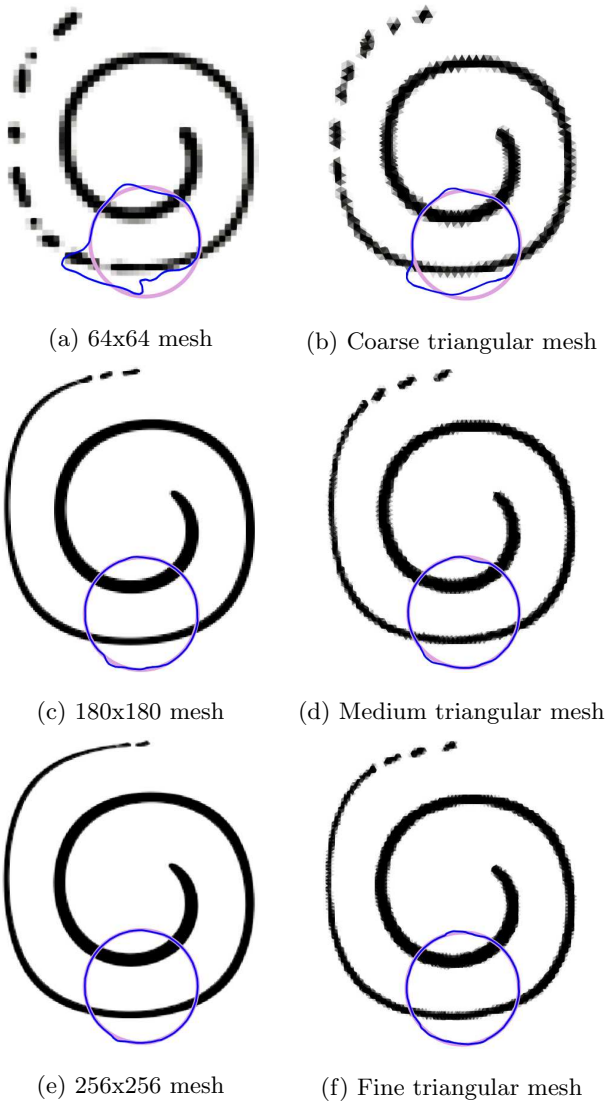

(a) 64x64 mesh (b) Coarse triangular mesh

(c) 180x180 mesh (d) Medium triangular mesh

(e) 256x256 mesh (f) Fine triangular mesh

Figure 5: Two-dimensional rotating disc test for level set-VOF method at $t = T/2$. The initial (light purple line) at $t = 0$ and final position of the zero-level set iso-surface (blue line) at $t = T$ are indicated.

Comparisons with different grid resolutions $(32^2, 64^2, 128^2)$ are shown in Table 4 for the values of the calculated $L_1(\alpha)$ error norm for the volume fraction. Results for $L_1(\alpha)$ from other numerical works are included for comparisons and

Table 2: Comparison of the methods using quadrilateral meshes for the two-dimensional rotating disc case.

Mesh resolution	ILSVOF method			VOF method		
	E_a	$\min(\alpha)$	$\max(\alpha)$	E_a	$\min(\alpha)$	$\max(\alpha)$
64^2	-1.03×10^{-7}	0.0	1.0	3.30×10^{-7}	0.0	1.0
180^2	-1.58×10^{-8}	4.60×10^{-9}	1.0	1.2×10^{-8}	-2.88×10^{-8}	$1.0\text{-}1.18\times10^{-8}$
256^2	-9.61×10^{-9}	-7.16×10^{-7}	$1.0\text{-}1.5\times10^{-9}$	-2.48×10^{-8}	-3.34×10^{-5}	$1.0\text{-}3.64\times10^{-8}$

Table 3: Comparisons of the methods using triangular meshes for the two-dimensional rotating disc case.

Mesh resolution	ILSVOF method			VOF method		
	E_a	$\min(\alpha)$	$\max(\alpha)$	E_a	$\min(\alpha)$	$\max(\alpha)$
17521	-2.77×10^{-7}	0.0	1.0	7.26×10^{-7}	-1.14×10^{-8}	$1.0\text{-}9.61\times10^{-10}$
79877	3.91×10^{-8}	0.0	1.0	-4.34×10^{-7}	0	1.0
108151	2.11×10^{-8}	0.0	1.0	-1.68×10^{-8}	-9.2×10^{-8}	$1.0\text{-}4.78\times10^{-8}$

the domain and physical properties for the rotating disc test are set as those in [57]. The method presented here, overall demonstrated good accuracy for the two-dimensional rotating vortex case. Compared to other volume of fluid methods that use PLIC such that in [6] the error in $L_1(\alpha)$ is lower for all the meshes tested here. Compared to the tangent of hyperbola for INterface capturing, (THINC) scheme and its variations [57–59], the results here are similar or lower. The $L_1(\alpha)$ error is close for the coarse mesh compared to the level set method in [60], but had lower values for the medium and fine meshes. The mass conservation error through time is shown in Fig. 8. The method showed generally reasonable mass conservation error for the different meshes that were used, as shown in Table 4.

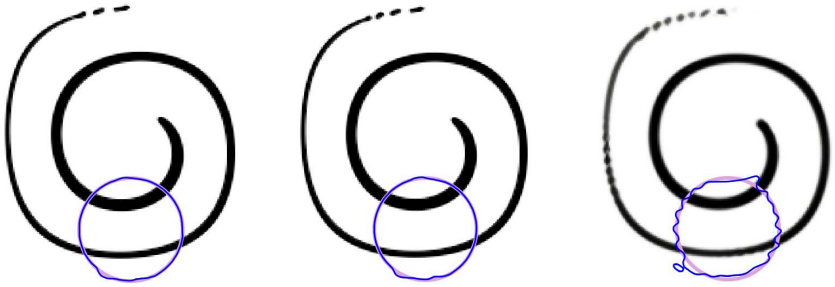

(a) Developed method (b) IsoAdvector VOF (c) VOF with MULES

Figure 6: Two-dimensional rotating disc test for the medium quadrilateral mesh at $t = T/2$. The initial (light purple line) at $t = 0$ and final position of the zero-level set iso-surface (blue line) at $t = T$ are indicated.

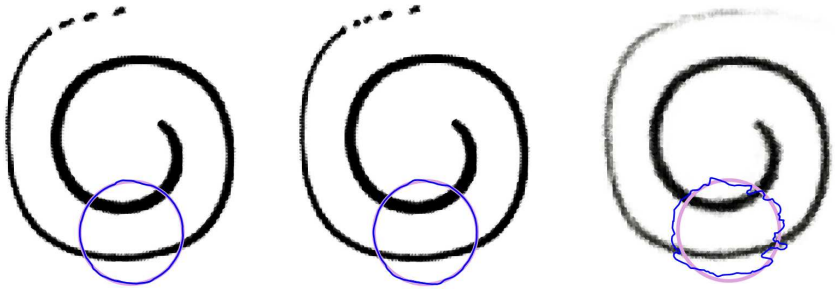

(a) Developed method (b) IsoAdvector VOF (c) VOF with MULES

Figure 7: Two-dimensional rotating disc test for the fine triangular mesh at $t = T/2$. Initial (light purple line) at $t = 0$ and final position of the zero-level set isosurface (blue line) at $t = T$ are indicated.

Table 4: Comparisons of the methods using quadrilateral meshes for the two-dimensional rotating disc case. The first order norm $L_1(\alpha)$ is calculated for the three different meshes.

Authors	32^2	64^2	128^2
RiderKothe/Puckett [61]	4.78×10^{-2}	6.96×10^{-3}	1.44×10^{-3}
THINC/WLIC [57]	4.16×10^{-2}	1.61×10^{-2}	3.56×10^{-3}
Markers-VOF [62]	7.41×10^{-3}	2.78×10^{-3}	4.78×10^{-4}
DS-CLSMOF [60]	2.92×10^{-2}	5.51×10^{-3}	1.37×10^{-3}
PLIC [6]	2.53×10^{-2}	2.78×10^{-3}	4.8×10^{-4}
THINC/QQ [58]	6.70×10^{-2}	1.52×10^{-2}	3.06×10^{-3}
THINC/SW scheme [59]	3.90×10^{-2}	1.52×10^{-2}	3.96×10^{-3}
ISLSVOF method	4.19×10^{-2}	1.43×10^{-3}	8.36×10^{-4}

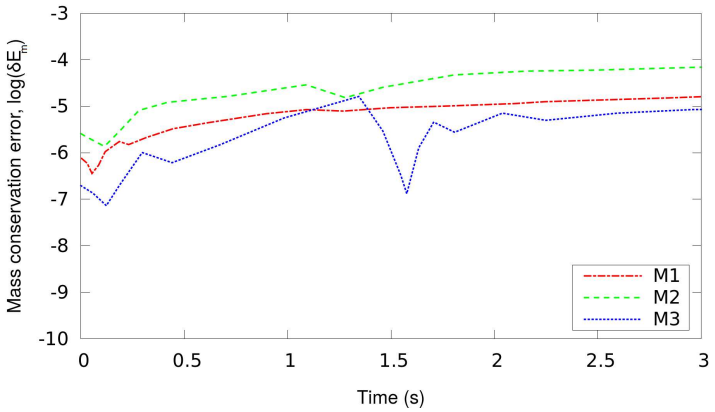

Figure 8: Mass conservation error for the two-dimensional rotating disc case for the three levels of refinement. Here, the meshes M_1, M_2 and M_3 had $32^2, 64^2$ and 128^2 cells respectively.

3.2. Three-dimensional rotating sphere in a non-uniform velocity field

The next test is the case of a three-dimensional rotating sphere of [54] and is used to assess the capability of the methodology for capturing the interface distortion in three dimensions. [34, 36, 42, 63]. In this test, a sphere with radius $R = 0.15m$ is placed inside a box $[0, 1]^3$ with its centre at $(0.35, 0.35, 0.35)$. The

velocity field is defined as

$$u(x,y,z,t) = 2sin^2(\pi x)sin(2\pi y)sin(2\pi z)cos\left(\frac{\pi t}{T}\right)$$
$$v(x,y,z,t) = -sin(2\pi x)sin^2(\pi y)sin(2\pi z)cos\left(\frac{\pi t}{T}\right) \quad (32)$$
$$w(x,y,z,t) = -sin(2\pi x)sin(2\pi y)sin^2(\pi z)cos\left(\frac{\pi t}{T}\right)$$

The period is $T = 3s$, and the density and viscosity of both fluids in the test, are the same as in the previous section (see Table 1). The sphere is rotating within the non-uniform velocity field which causes the sphere to deform through time during $[0, T/2]$. At $t = T/2$ the flow reverses due to the sign change of the cosine parameter during $[T/2, T]$ causing the deformed sphere to return back to its original position at $t = T$. The ILSVOF method was first tested for three different meshes (with $40^2, 64^2, 100^2$ elements) to assess the error in shape preservation and the boundedness of the marker function. The results given in Table 5 compare the method with and without the level set step using structured meshes. Overall, the error E_α decreases with the level set implementation. A slight increase in E_α is observed for the fine mesh with respect to the medium mesh, although this is relatively insignificant. Similar trends were observed by previous authors using LS and VOF method coupling [34]. A more detailed comparison is given in Fig. 9 at the maximum deformation time, $t = T/2$ for different grid resolutions ($40^2, 64^2, 100^2, 128^2$ elements). The deforming sphere appears to be thicker in the case of the ILSVOF method which provides more detail for the deforming sphere for the different levels of mesh refinement. The sharp sphere end is also thickened in the ILSVOF case, and the thickening appears to be more evident for the finer meshes. The time evolution of the deforming sphere inside the non-uniform flow is shown for different times within $[0, T]$ in Fig. 10 for a 128^3 mesh. Numerical results revealed as before, relatively large gradients that the LS function experiences in $[0, T/2]$ which are maintained and are not reversed in the interval $[T/2, T]$ giving a perturbed profile at the final position of the sphere. The sphere interface is distorted in all cases as shown in Fig 11 at $t = T$, with or without level set or interface compression. In general,

the ILSVOF method shows better representation of the surface. The most significant surface distortion is observed in the case of the interface compression where the compression of the interface decreases the solution accuracy [34]. The three-dimensional sphere in the same non-uniform flow was also simulated using unstructured meshes and the results are shown in Table 6. The values of E_α are higher for the medium and fine meshes compared with those in Table 5 for structured meshes. The sheet thickness appears to be smaller than the average edge length even for the finest tetrahedral mesh (~ 0.008), causing the solution accuracy to drop in the case of unstructured meshes. In addition, the impact of the steep gradients introduced in the LS method that originate from the initial value of ψ_0 in Eq. 22 being inserted in Eq. 3 are more evident in the case of tetrahedral meshes. The L_1 error for the volume fraction for different mesh resolutions ($32^3, 64^3, 128^3$) for the three-dimensional case of the rotating sphere are shown in Table 7. Following [56, 59] the error $L1$ is calculated for all cells i and is defined as

$$L_1(\alpha) = \sum_i (\alpha_i - \alpha_{exact}) V_i \tag{33}$$

The results are shown alongside with the L_1 error obtained with other volume of fluid methods. The accuracy of the results here, remained lower than the volume of fluid with the THINC/SW scheme which uses no geometrical reconstruction [59] and was more accurate compared to the results obtained in [56] with the MULES limiter with interFoam. In all cases the L_1 error was very close to the results from the PLIC VOF method in [64].

Table 5: Comparison of the methods using quadrilateral meshes for the three-dimensional rotating sphere case.

Grid	ILSVOF method			VOF method		
	E_a	$\min(\alpha)$	$\max(\alpha)$	E_a	$\min(\alpha)$	$\max(\alpha)$
40^3	5.43×10^{-7}	-4.05×10^{-17}	1.0	5.84×10^{-7}	-1.87×10^{-16}	1.0
64^3	-9.85×10^{-8}	-1.48×10^{-16}	1.0 -2.22×10^{-16}	-1.04×10^{-7}	-1.53×10^{-9}	1.0-5.93×10^{-11}
100^3	1.79×10^{-7}	0.0	1.0	3.22×10^{-7}	0.0	1.0

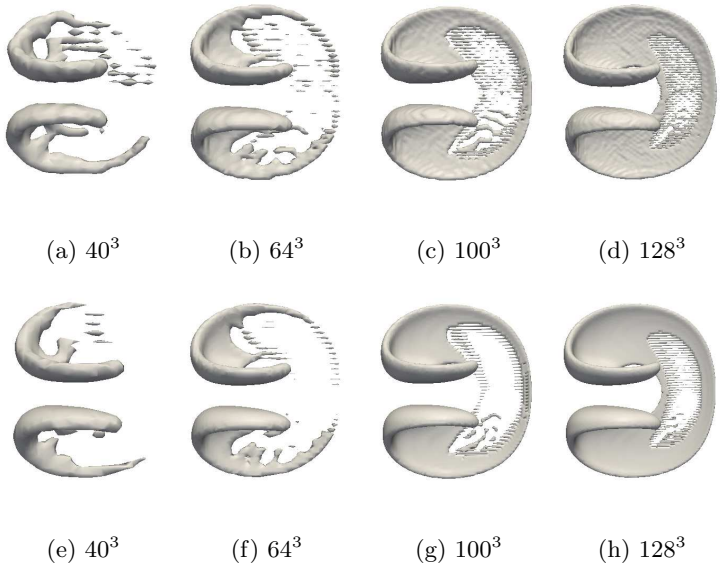

(a) 40^3 (b) 64^3 (c) 100^3 (d) 128^3

(e) 40^3 (f) 64^3 (g) 100^3 (h) 128^3

Figure 9: Three-dimensional rotating sphere in a non-uniform flow test for various levels of mesh. The 0.5-iso-surface obtained with the ILSVOF method (top) and without the level set step (bottom) are shown at the maximum deformation time, $t = T/2$.

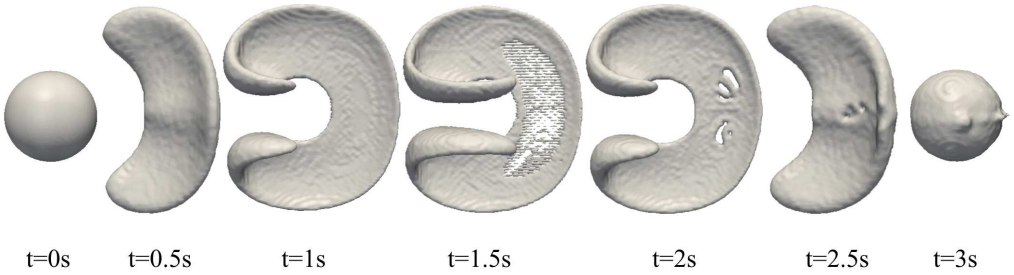

Figure 10: Three-dimensional rotating sphere in a non-uniform flow during time evolution in $[0, T]$ for a fine hexahedral mesh of 128^3 hexahedra.

(a) Developed method ILSVOF.

(b) Isoface method without level set.

(c) Interface compression scheme, MULES.

Figure 11: Three-dimensional rotating sphere in a non-uniform flow test using the 128^3 hexahedral mesh. Initial transparent blue surface at $t = 0$ and final position of the zero-level set iso-surface solid grey iso-surface at $t = T$.

3.3. Three-dimensional dam break case without obstacle

The dam break problem is studied next which consists of a simple three-dimensional rectangular geometry wherein a liquid column is initially held still by a dam. When the dam is suddenly removed, the liquid column collapses. The tank containing the liquid column which collapses in this case is a rectangular

Table 6: Comparison of the methods using tetrahedral meshes for the three-dimensional rotating sphere case.

Mesh resolution	ILSVOF method			VOF method		
	E_a	$\min(\alpha)$	$\max(\alpha)$	E_a	$\min(\alpha)$	$\max(\alpha)$
163208	-6.42×10^{-8}	0	1.0	2.68×10^{-8}	0.0	1.0
322676	-8.7×10^{-3}	0.0	1.0	-3.78×10^{-3}	0.0	1.0
1083126	-2.3×10^{-4}	0.0	1.0	-7.8×10^{-3}	0.0	1.0

Table 7: $L_1(\alpha)$ error norm for different meshes for the three-dimensional rotating sphere case and comparison with other numerical methods.

Authors	32^3	64^3	128^3
RK-3D using PLIC [64]	7.85×10^{-3}	2.75×10^{-3}	7.41×10^{-4}
THINC/SW scheme [59]	8.39×10^{-3}	3.47×10^{-3}	1.08×10^{-3}
interFoam [56]	9.95×10^{-3}	4.78×10^{-3}	2.03×10^{-3}
ISLSVOF method	8.89×10^{-3}	2.96×10^{-3}	8.06×10^{-4}

domain with dimensions $4a \times 2.4a \times a$. For a more convenient comparison, the fluid in the liquid column is assumed to be water and the rest of the tank is filled with air. Both fluids are assumed to be initially still, and the physical properties of the three-dimensional case are shown in Table 8. Initially the liquid column has dimensions $a \times 2a \times a$. The vertical acceleration due to gravity is taken to be 9.81 ms^{-2}. The velocity before removing the dam, is zero for the liquid column and the air, and the pressure is set to be the hydrostatic pressure. Free slip boundary conditions are imposed for all the boundaries of the domain (assuming zero normal velocity and zero tangential traction) except for the open top boundary (where the tangential velocity and normal traction are zero). The displacement of the interface between water and air is tracked in order to characterise the performance of the developed method using three different grids ($40 \times 10 \times 20$, $80 \times 20 \times 40$ and $160 \times 40 \times 80$). The results are compared with the experimental data available in [65] and previous numerical studies using the LS method from [66] which is a conservative level set method based on the finite element approach which employs the volume fraction for correcting the distance function. The results for the position of the water-air interface along the horizontal (x-axis) and the vertical (y-axis) directions are shown in Fig. 12. The results for the position are normalised with the length parameter a and are plotted against the non-dimensional time. The predictions for the leading-edge position are in good agreement with the experimental data for the examined time interval. The accuracy in the predictions for the horizontal direction is closer initially and reasonably close to the experiment during the simulation until the leading edge reaches the wall, $x/a = 4$. The flow slows down as a result of wall friction as reported in the experimental work and, as a result, the calculated interface is expected to differ from the experiment, although this is less than five to ten percent here for the fine and coarse meshes respectively. The interface in [66] reaches the position $x/a = 4$ faster than the present simulations here. In the method presented here, the liquid front propagates slower than in [66] although the results in [66] for a coarse mesh (not shown here) had similar trends as for the results obtained here for the different grids. The coarse grid

results in the present study are close to the liquid front results reported in [65], with the results obtained with the other two meshes also being reasonably close to the experiment. The time evolution of the interface is shown in Figs.13. The shape of the interface remains almost flat for the considered time steps of the experiment, and in Fig.13(a-c). Once the collapsing liquid column reaches the wall, the water rises upwards forming a layer on the right wall. During the time interval $[0, 0.26s]$ the vertical position of the interface decreases as expected, and both the present method and the results of Kees et al.[66] are seen to be very close in Fig. 12b, having the same rate of change in the liquid column height for the different grid resolutions. The fluid percent mass loss evolution for the dam break case is shown in Fig. 14. The mass loss approaches zero for the fine mesh and remains less than 0.01 percent for the coarse mesh.

Table 8: Physical properties for the dam break case.

	Physical and numerical parameters
Water density	1000 kg/m^3
Air density	1.0 kg/m^3
Water kinematic viscosity	1.0e-06 m^2/s
Air kinematic viscosity	1.0e-04 m^2/s
Length a	0.146 m
CFL number	0.5

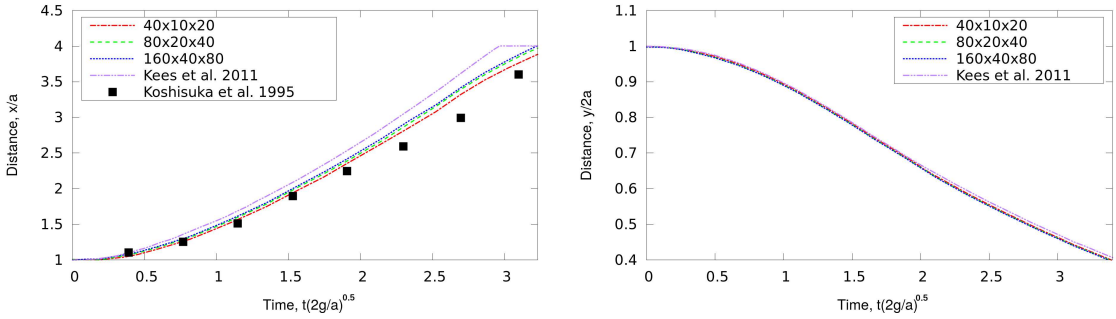

(a) X-axis. (b) Y-Axis.

Figure 12: Water-air interface position along the x-axis and y-axis for the three-dimensional dam break case without obstacle.

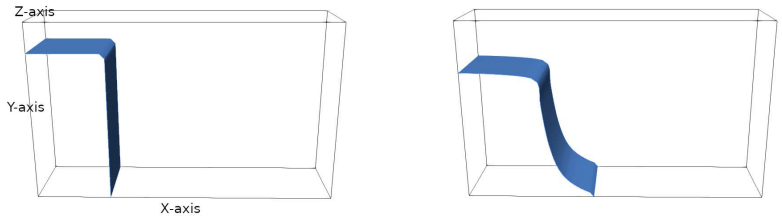

(a) t=0s (b) t=0.1s

(c) t=0.2s (d) t=0.3s

(e) t=0.4s

Figure 13: 0.5-isosurface snapshots at different times for the three-dimensional dam break case without obstacle. The liquid column starts to collapse at t=0s and moves towards the right wall until it impinges and rises up forming a layer that keeps moving upwards until it returns back to the tank due to gravity.

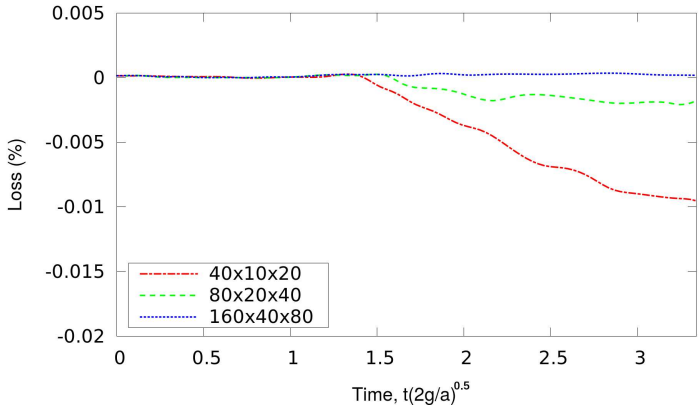

Figure 14: Percent mass loss for the dam break case through time for different mesh resolutions.

3.4. Static drop

In this test case we are interested in the verification of the methodology for the stationary Laplace solution for a droplet inside a closed domain and assessing the spurious currents [29, 67]. Neglecting any gravitational effects and any external forces the interface between the drop and the ambient fluid is expected to remain at rest. The surface tension force ($\sigma\kappa$) is balanced by the pressure force at the interface according to Laplace's law: $\Delta p_{exact} = \sigma\kappa_{exact}$, where the exact interface curvature is $\kappa = 2/d$ and σ is the surface tension. For a constant pressure outside the droplet p_0 and zero velocity, the pressure inside remains constant and equal to $p_0 + 2\sigma/d$. Due to spurious currents the calculated pressure will differ. A $2d \times 2d$ domain was used for the present numerical tests with $d = 0.5cm$ and the density ratio between the droplet and the surroundings was 10^4. The viscosities inside and outside were equal to 1 and the surface tension was $1kg \cdot s^{-2}$. For the two-dimensional tests, three meshes of triangular elements were used (with grid size $\Delta x = 1/25, 1/50, 1/100$ as in [29]). In order to evaluate the parasitic currents in the domain, the L_1 error norm is calculated as

$$L_1(\mathbf{u}) = \frac{1}{N_c}\sum_i (\mathbf{uu})^{1/2}\frac{\mu}{\sigma} \tag{34}$$

where the summation is done over the entire domain as in [29] and [68]. The pressure ranges from p_{out} (pressure outside the droplet) to the inside pressure (p_{in}). The pressure error used to evaluate the pressure jump denoted by $E(\Delta p)$, is

$$E(\Delta p) = \frac{|p_{in} - p_{out} - 2\sigma/d|}{2\sigma/d} \tag{35}$$

The calculated values for L_1 and $E(\Delta p)$ for the three meshes are shown in Table 9. The results are also compared to the ones obtained using the VOF only without using level set and the CLSVOF in [29] using PLIC. The parasitic currents obtained here are close to those in [29] and smaller than the VOF approach. In all cases the error L_1 decreases when increasing the mesh resolution. Similar behaviour is observed for the $E(\Delta p)$ which remained smaller than the calculated error values for pressure jump reported in [29] for the different grid resolutions. Fig.15 shows the pressure jump for the three different meshes compared to the exact solution (normalised with the maximum pressure difference Δp_0). Overall the calculated pressure is close enough to the exact value.

Another values that are also used for the static drop test are the L_1 error norm for pressure, $L_1(p)$ and the maximum velocity after one and fifty time-steps $U_{max,1}, U_{max,50}$. The drop density for the test is set to $1000 kgm^{-3}$ with a density ratio with the ambient gas phase equal to 1000. The rest of the properties for the drop and the outside are set as in [68]. For this test, the drop has a radius $R = 2cm$ and is placed at the centre of a $6cm \times 6cm$ square domain. Three different grid resolutions were used for this case, with grid size Δx such that $R/\Delta x = 10, 20, 40$ and the results are shown in Table 10. The order for the $L_1(p)$ error remains at the order of 10^{-4} or below and the accuracy of the presented method was close to the CLSVOF works in [68] and [55]. The unphysical velocity fields that occur in the areas where pressure changes are monitored using the maximum velocity U_{max}. In this study U_{max} was of order

Table 9: Comparisons of the methods using unstructured meshes for the two-dimensional static drop case.

Mesh resolution	ILSVOF method		VOF method		CLSVOF using PLIC [29]	
	$L_1(\mathbf{u})$	$E(\Delta p)$	$L_1(\mathbf{u})$	$E(\Delta p)$	$L_1(\mathbf{u})$	$E(\Delta p)$
1/25	1.24×10^{-4}	0.011	5.84×10^{-3}	0.026	1.3×10^{-4}	0.02433
1/50	9.81×10^{-6}	0.0046	3.76×10^{-5}	0.0078	3.19×10^{-5}	0.00651
1/100	7.46×10^{-6}	0.0017	6.61×10^{-5}	0.0049	8.82×10^{-6}	0.00215

of 10^{-8} for the coarser mesh and was higher for the finer meshes, at the order of 10^{-7} as in [67]. Similar patterns for higher parasitic currents while increasing the mesh resolution were also reported before in [68], [55] and [67] and has been reported for different VOF methods which employ the continuous surface force model [50].

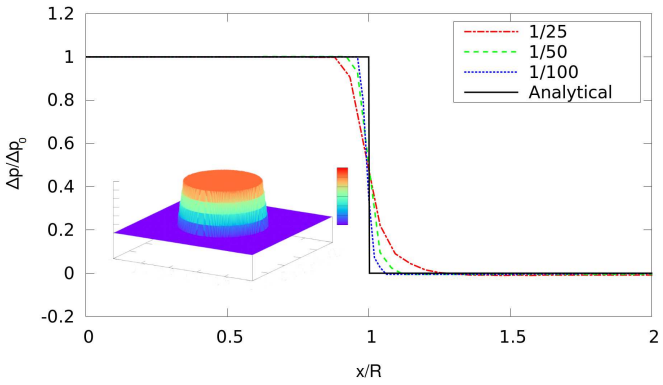

Figure 15: Distribution of the pressure for the static drop test case. Three different mesh resolutions are used to capture the pressure jump across the interface. The pressure is normalised with the exact value Δp_0 and the distance with the droplet radius R. The distribution of the pressure for the finest mesh is also shown.

Table 10: Convergence study for the calculation of pressure, pressure error and velocity for the static drop test. Three different mesh resolutions are used and the density ratio was 1000 on three different grids. Results are compared with different numerical studies.

Authors	$R/\Delta x$	$L_1(p)$	$\lvert u_{max,1}\rvert$	$\lvert u_{max,50}\rvert$
Gerland et al. 2006 [68]	10	4.81×10^{-3}	7.82×10^{-8}	3.91×10^{-6}
	20	9.48×10^{-4}	1.70×10^{-7}	8.53×10^{-6}
	40	7.04×10^{-5}	4.34×10^{-7}	2.17×10^{-5}
Ningegowda et al. 2014 [55]	10	1.14×10^{-2}	1.12×10^{-6}	5.11×10^{-5}
	20	7.53×10^{-3}	5.88×10^{-6}	3.10×10^{-4}
	40	2.92×10^{-3}	1.30×10^{-5}	9.43×10^{-4}
Jarauta et al. 2018 [67]	10	1.25×10^{-4}	6.08×10^{-9}	4.09×10^{-7}
	20	3.12×10^{-4}	4.38×10^{-8}	1.22×10^{-6}
	40	7.85×10^{-5}	4.26×10^{-7}	3.55×10^{-6}
ISLSVOF method	10	7.36×10^{-4}	2.36×10^{-8}	8.89×10^{-6}
	20	1.66×10^{-4}	5.41×10^{-8}	3.46×10^{-6}
	40	8.21×10^{-5}	7.22×10^{-7}	1.17×10^{-6}

3.5. Rising bubble

The final test case is the rising bubble test proposed in [69]. A circular bubble is initially placed in a column filled with fluid of higher density than the density of bubble. Due to the buoyancy force, the bubble rises and deforms while moving towards the top of the column. The bubble diameter is initially $d = 0.5$ units and is centred at $(0.5, 0.5)$ in a rectangular domain with dimensions $2d \times 4d$ as in Fig.16. At the bottom and the top of the column a no-slip boundary condition is applied with a free-stream boundary condition at the vertical walls of the domain. The velocity is set to zero in the domain, and inside the bubble the pressure is constant. The physical properties for the bubble and the heavier surrounding fluid are listed in Table 11. Different triangular meshes were used with their resolution varying as: $d/40, d/80, d/160$. The benchmark quantities used by [69] are the centre mass (y_c), the rise velocity of the bubble (v_c) and its circularity or sphericity in three dimensions (ζ). These are defined as

$$
\begin{aligned}
y_c &= \frac{\int_{\Omega_b} \mathbf{x} dV}{\int_{\Omega_b} dV} \\
v_c &= \frac{\int_{\Omega_b} \mathbf{u} dV}{\int_{\Omega_b} dV} \\
\zeta &= \frac{\pi d}{\Pi}
\end{aligned}
\tag{36}
$$

where Ω_b is the region occupied by the bubble and Π is the perimeter of the bubble. Fig.17 shows the benchmark quantities through time for the different meshes. Results obtained in the present study are close to the values obtained in [69] and [70] for x_c, v_c and ζ for the different mesh resolutions. For the present conditions with $Re = 35$ and $Eo = 10$, where $Eo = gd^2\Delta\rho/\sigma$ is the Eötvös number, the surface tension force is significant which prevents the bubble disintegrating. The bubble deforms ($t = 1$) and changes shape from circular to ellipsoid (see also [70]) reaching its terminal velocity at $t = 2$ which is approximately 90 percent of the maximum bubble velocity. The change in rise velocity is in good agreement with the velocity obtained in [70]. At the change in circularity at $t = 1.9$ where the surface tension effect on the bubble shape is

more evident, and is captured with all three computational meshes in this study and is also in close agreement with the calculated ζ in [69]. Similar patterns for the calculated benchmark quantities were also observed in other numerical works [29, 33, 70]. The results for the relative error norms for y_c, ζ and v_c are shown in Table 12. The calculated errors are in close agreement with the results reported in [70] for the three benchmark quantities.

For the three-dimensional version of rising bubble test case, a three-dimensional bubble is placed in a cylinder with height $8d$ and diameter $8d$. The bubble is placed at a distance $1.5d$ from the bottom of the cylinder. The density and viscosity ratio between the bubble and the surrounding fluid were set to 100. Three hexahedral meshes with different resolution were used for this study, with a grid size $\Delta x = d/15, 20, 40$. The errors E_{Re} and E_{ζ} for the calculated Reynolds number Re and sphericity ζ are used to assess the accuracy of the method, where $E_{Re} = (Re - Re_{exact})/Re_{exact}$, $E_{\zeta} = (\zeta - \zeta_{exact})/\zeta_{exact}$ (where Re_{exact} and ζ_{exact} are the exact values for Re and ζ respectively). The results shown in Table 13 are in good agreement for the three meshes compared to the results from the reference case in [29]. In Fig.18 the mass conservation error is shown through time. The mass conservation error is calculated with respect to the volume fraction at $t = 0$, $\alpha(0)$ and is defined following [29] as $\delta M = |\alpha - \alpha(0)|/\alpha(0)$. The error for the different meshes remained of the order of 10^{-5} or below showing reasonable accuracy for mass conversation. A similar order for δM is reported in the CLSVOF work in [29].

Table 11: Physical properties for the two-dimensional rising bubble test case.

	Physical and numerical parameters
Heavy fluid density	1000 kg/m^3
Bubble density	100 kg/m^3
Heavy fluid viscosity	10 $kg/m \cdot s$
Bubble fluid viscosity	1 $kg/m \cdot s$

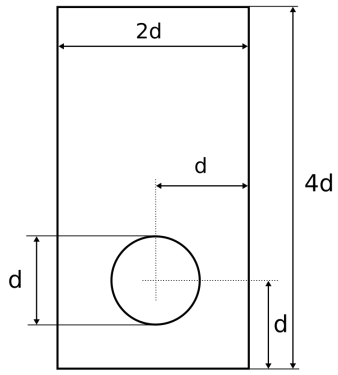

Figure 16: Domain for the two-dimensional bubble rise test case. The diameter of the bubble is initially $d = 0.5$.

Table 12: Relative norm error for the centre of mass, circularity and velocity of the bubble in the two-dimensional rising bubble case. Three different structured meshes are used, and the results are compared with the level set method of [70].

Mesh size	ILSVOF method			LS method of [70]		
	Centre of mass	Circularity	Velocity	Centre of mass	Circularity	Velocity
1/40	1.79×10^{-3}	1.19×10^{-3}	1.06×10^{-2}	2.65×10^{-3}	1.0×10^{-3}	1.19×10^{-2}
1/80	8.91×10^{-4}	3.18×10^{-4}	1.81×10^{-3}	9.64×10^{-4}	3.01×10^{-4}	2.9×10^{-3}
1/160	2.41×10^{-4}	6.37×10^{-5}	6.21×10^{-4}	2.62×10^{-4}	8.83×10^{-5}	7.73×10^{-4}

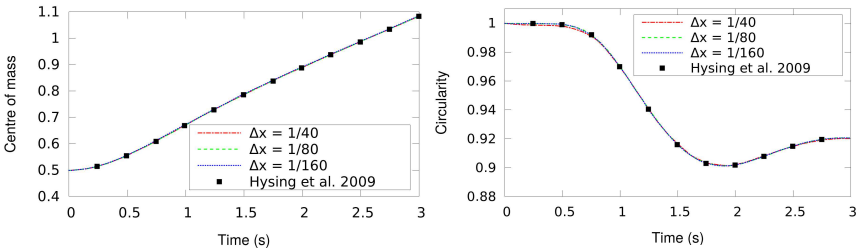

(a) Centroid.

(b) Circularity.

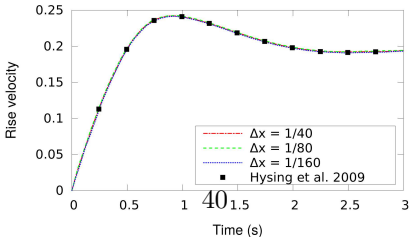

(c) Rise velocity.

Figure 17: Evolution of rising bubble benchmark quantities through time. The results are compared with the case in [70].

Table 13: Error for Re and sphericity of the bubble in the three-dimensional rising bubble case. Three different structured meshes are used and the results are compared with the CLSVOF method of [29].

Mesh size	ILSVOF method		CLSVOF method of [29]	
	E_{Re}	E_{ζ}	E_{Re}	E_{ζ}
$d/15$	0.00363	0.0126	0.00341	0.0118
$d/20$	0.00314	0.0063	0.00339	0.0074
$d/40$	0.00271	0.0036	-	-

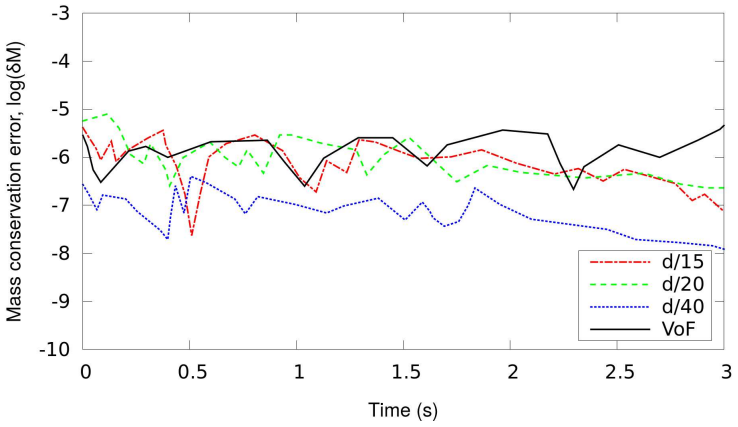

Figure 18: Mass conservation error for three-dimensional rising bubble case for the three levels of refinement.

4. Conclusions

A novel method for simulating the flow of two immiscible fluids tracking their interface is presented coupling the level set and volume of fluid methods. The new ILSVOF method involves a novel re-initialisation methodology which is described in detail. ILSVOF is simple and can be readily implemented for any type of polyhedral unstructured mesh. A smooth calculation of the gradient of the LS function is utilised considering the neighbouring cells via an

interpolation at the cell-faces. Using these cell-face calculations for each interface cell, it is easy to overcome the limitation of having to arbitrarily define the upwind and downwind cells. The initial value for the re-distancing algorithm is obtained via the advection of the isoface within a time step instead of by using an algebraic method. Overall, the method provides better accuracy compared to the VOF method in most of the numerical tests considered and has been demonstrated to give an accurate representation of the interface in both two and three-dimensional test cases. The mapping of the volume fraction to the distance function is extremely important for the re-initialisation procedure, and alternative ways of doing this, such as by employing a special advection step within each solution time step, should be further investigated. Further comparisons with high order level set approaches could also be used to improve the level set advection step.

Acknowledgments

The authors would like to thank the EU project GENIORS (Project ID: 755171) on GEN IV Integrated Oxide Fuels Recycling Strategies and the EPSRC project PACIFIC (EP/L018616/1) for funding this research.

References

[1] C. W. Hirt, B. D. Nichols, Volume of fluid (vof) method for the dynamics of free boundaries, Journal of Computational Physics 39 (1981) 201 – 225.

[2] B. Lafaurie, C. Nardone, R. Scardovelli, S. Zaleski, G. Zanetti, Modelling merging and fragmentation in multiphase flows with surfer, Journal of Computational Physics 113 (1994) 134–147.

[3] R. Scardovelli, S. Zaleski, Direct numerical simulation of free-surface and interfacial flow, Annual review of fluid mechanics 31 (1999) 567–603.

[4] D. Gueyffier, J. Li, A. Nadim, R. Scardovelli, S. Zaleski, Volume-of-fluid interface tracking with smoothed surface stress methods for three-dimensional flows, Journal of Computational physics 152 (1999) 423–456.

[5] R. Scardovelli, S. Zaleski, Analytical relations connecting linear interfaces and volume fractions in rectangular grids, Journal of Computational Physics 164 (2000) 228–237.

[6] E. Aulisa, S. Manservisi, R. Scardovelli, S. Zaleski, A geometrical area-preserving volume-of-fluid advection method, Journal of Computational Physics 192 (2003) 355–364.

[7] G. Tryggvason, R. Scardovelli, S. Zaleski, Direct numerical simulations of gas–liquid multiphase flows, Cambridge University Press, 2011.

[8] G. Agbaglah, S. Delaux, D. Fuster, J. Hoepffner, C. Josserand, S. Popinet, P. Ray, R. Scardovelli, S. Zaleski, Parallel simulation of multiphase flows using octree adaptivity and the volume-of-fluid method, Comptes Rendus Mecanique 339 (2011) 194–207.

[9] M. Owkes, O. Desjardins, A computational framework for conservative, three-dimensional, unsplit, geometric transport with application to the volume-of-fluid (vof) method, Journal of Computational Physics 270 (2014) 587–612.

[10] Y. Ling, S. Zaleski, R. Scardovelli, Multiscale simulation of atomization with small droplets represented by a lagrangian point-particle model, International Journal of Multiphase Flow 76 (2015) 122–143.

[11] S. Bnà, S. Manservisi, R. Scardovelli, P. Yecko, S. Zaleski, Vofia library to initialize the volume fraction scalar field, Computer Physics Communications 200 (2016) 291–299.

[12] S. Osher, J. A. Sethian, Fronts propagating with curvature-dependent speed: Algorithms based on hamilton-jacobi formulations, Journal of Computational Physics 79 (1988) 12–49.

[13] B. Merriman, J. K. Bence, S. J. Osher, Motion of multiple junctions: A level set approach, Journal of Computational Physics 112 (1994) 334–363.

[14] Y.-C. Chang, T. Hou, B. Merriman, S. Osher, A level set formulation of eulerian interface capturing methods for incompressible fluid flows, Journal of computational Physics 124 (1996) 449–464.

[15] J. A. Sethian, Level set methods, evolving interfaces in geometry, fluid mechanics comuputer vision, and materials sciences, Cambridge Monographs on Applied and Computational Mathematics, 3 (1996).

[16] J. A. Sethian, Level set methods and fast marching methods: evolving interfaces in computational geometry, fluid mechanics, computer vision, and materials science, volume 3, Cambridge university press, 1999.

[17] S. Osher, R. P. Fedkiw, Level set methods: an overview and some recent results, Journal of Computational physics 169 (2001) 463–502.

[18] D. Enright, R. Fedkiw, J. Ferziger, I. Mitchell, A hybrid particle level set method for improved interface capturing, Journal of Computational physics 183 (2002) 83–116.

[19] J. A. Sethian, P. Smereka, Level set methods for fluid interfaces, Annual review of fluid mechanics 35 (2003) 341–372.

[20] S. Osher, R. Fedkiw, Level set methods and dynamic implicit surfaces, volume 153, Springer Science & Business Media, 2006.

[21] J. A. Sethian, A. Wiegmann, Structural boundary design via level set and immersed interface methods, Journal of computational physics 163 (2000) 489–528.

[22] S. Osher, N. Paragios, Geometric level set methods in imaging, vision, and graphics, Springer Science & Business Media, 2003.

[23] R. Malladi, J. A. Sethian, Image processing via level set curvature flow, proceedings of the National Academy of sciences 92 (1995) 7046–7050.

[24] W. Dawes, S. Harvey, W. Kellar, Using level sets as the basis for a scalable, parallel geometry engine and mesh generation system, in: 47th AIAA Aerospace Sciences Meeting including The New Horizons Forum and Aerospace Exposition, 2009, p. 372.

[25] M. K. Cameron, S. B. Fomel, J. A. Sethian, Seismic velocity estimation from time migration, Inverse Problems 23 (2007) 1329.

[26] J. A. Sethian, Y. Shan, Solving partial differential equations on irregular domains with moving interfaces, with applications to superconformal electrodeposition in semiconductor manufacturing, Journal of Computational Physics 227 (2008) 6411–6447.

[27] A. Bourlioux, A coupled level set and volume of fluid algorithm for tracking material interfaces, Proceedings of the 6th International Symposium On Computational Fluid Dynamics 6 (1995) 15–22.

[28] M. Sussman, E. G. Puckett, A coupled level set and volume-of-fluid method for computing 3d and axisymmetric incompressible two-phase flows, Journal of Computational Physics 162 (2000) 301–337.

[29] N. Balcázar, O. Lehmkuhl, L. Jofre, J. Rigola, A. Oliva, A coupled volume-of-fluid/level-set method for simulation of two-phase flows on unstructured meshes, Computers and Fluids 124 (2016) 12 – 29.

[30] Z. Cao, D. Sun, J. Wei, B. Yu, A coupled volume-of-fluid and level set method based on multi-dimensional advection for unstructured triangular meshes, Chemical Engineering Science 176 (2018) 560 – 579.

[31] D. L. Sun, W. Q. Tao, A coupled volume-of-fluid and level set (voset) method for computing incompressible two-phase flows, International Journal of Heat and Mass Transfer 53 (2010) 645 – 655.

[32] Y. Zhao, H. C. Chen, A new coupled level set and volume-of-fluid method to capture free surface on an overset grid system, International Journal of Multiphase Flow 90 (2017) 144 – 155.

[33] N. K. Singh, B. Premachandran, A coupled level set and volume of fluid method on unstructured grids for the direct numerical simulations of two-phase flows including phase change, International Journal of Heat and Mass Transfer 122 (2018) 182 – 203.

[34] M. Dianat, M. Skarysz, A. Garmory, A coupled level set and volume of fluid method for automotive exterior water management applications, International Journal of Multiphase Flow 91 (2017) 19 – 38.

[35] E. Olsson, G. Kreiss, A conservative level set method for two phase flow, Journal of Computational Physics 210 (2005) 225–246.

[36] A. Albadawi, D. B. Donoghue, A. J. Robinson, D. B. Murray, Y. M. C. Delaur, Influence of surface tension implementation in volume of fluid and coupled volume of fluid with level set methods for bubble growth and detachment, International Journal of Multiphase Flow 53 (2013) 11 – 28.

[37] T. Pringuey, Large eddy simulation of primary liquid sheet breakup, Ph.D. thesis, University of Cambridge, 2012.

[38] L. H. Zhao, J. Mao, X. Q. Liu, X. Bai, J. Willims, Improved conservative level set method for free surface flow simulation, Journal of Hydrodynamics, Ser. B 26 (2014) 316 – 325.

[39] M. Sussman, P. Smereka, S. Osher, A level set approach for computing solutions to incompressible two-phase flow, Journal of Computational Physics 114 (1994) 146–159.

[40] G. Russo, P. Smereka, A remark on computing distance functions, Journal of Computational Physics 163 (2000) 51–67.

[41] D. Hartmann, M. Meinke, W. Schröder, Differential equation based constrained reinitialization for level set methods, Journal of Computational Physics 227 (2008) 6821 – 6845.

[42] J. Roenby, H. Bredmose, H. Jasak, A computational method for sharp interface advection, Royal Society open science (2016).

[43] H. G. Weller, G. Tabor, H. Jasak, C. Fureby, A tensorial approach to computational continuum mechanics using object-oriented techniques, Comput. Phys. 12 (1998) 620–631.

[44] X. D. Liu, S. Osher, T. Chan, Weighted essentially non-oscillatory schemes, Journal of Computational Physics 115 (1994) 200–212.

[45] H. Weller, A new approach to vof-based interface capturing methods for incompressible and compressible flow, OpenCFD Ltd technical report (2008).

[46] A. Prosperetti, G. Tryggvason, Computational Methods for Multiphase Flow, Cambridge University Press, 2009.

[47] D. Hartmann, M. Meinke, W. Schröder, The constrained reinitialization equation for level set methods, Journal of Computational Physics 229 (2010) 1514–1535.

[48] C. Dapogny, P. Frey, Computation of the signed distance function to a discrete contour on adapted triangulation, Calcolo 49 (2012) 193–219.

[49] C. Kunkelmann, P. Stephan, Modification and extension of a standard volume-of-fluid solver for simulating boiling heat transfer, ECCOMAS CFD2010, 2010.

[50] J. U. Brackbill, D. B. Kothe, C. Zemach, A continuum method for modeling surface tension, Journal of computational physics 100 (1992) 335–354.

[51] M. Rudman, Volume-tracking methods for interfacial flow calculations, International Journal for Numerical Methods in Fluids 24 (1997) 671–691.

[52] N. Ashgriz, J. Y. Poo, Flair: Flux line-segment model for advection and interface reconstruction, Journal of Computational Physics 93 (1991) 449 – 468.

[53] J. E. Pilliod, E. G. Puckett, Second-order accurate volume-of-fluid algorithms for tracking material interfaces, Journal of Computational Physics 199 (2004) 465 – 502.

[54] R. J. LeVeque, High-resolution conservative algorithms for advection in incompressible flow, SIAM J. Numer. Anal. 33 (1996) 627–665.

[55] B. Ningegowda, B. Premachandran, A coupled level set and volume of fluid method with multi-directional advection algorithms for two-phase flows with and without phase change, International Journal of Heat and Mass Transfer 79 (2014) 532–550.

[56] S. S. Deshpande, L. Anumolu, M. F. Trujillo, Evaluating the performance of the two-phase flow solver interfoam, Computational Science & Discovery 5 (2012) 014016.

[57] K. Yokoi, Efficient implementation of thinc scheme: a simple and practical smoothed vof algorithm, Journal of Computational Physics 226 (2007) 1985–2002.

[58] B. Xie, F. Xiao, Toward efficient and accurate interface capturing on arbitrary hybrid unstructured grids: The thinc method with quadratic surface representation and gaussian quadrature, Journal of Computational Physics 349 (2017) 415–440.

[59] F. Xiao, S. Ii, C. Chen, Revisit to the thinc scheme: a simple algebraic vof algorithm, Journal of Computational Physics 230 (2011) 7086–7092.

[60] M. Jemison, E. Loch, M. Sussman, M. Shashkov, M. Arienti, M. Ohta, Y. Wang, A coupled level set-moment of fluid method for incompressible two-phase flows, Journal of Scientific Computing 54 (2013) 454–491.

[61] W. J. Rider, D. B. Kothe, Reconstructing volume tracking, Journal of computational physics 141 (1998) 112–152.

[62] J. Lopez, J. Hernandez, P. Gomez, F. Faura, An improved plic-vof method for tracking thin fluid structures in incompressible two-phase flows, Journal of Computational Physics 208 (2005) 51–74.

[63] T. Ménard, S. Tanguy, A. Berlemont, Coupling level set/vof/ghost fluid methods: Validation and application to 3d simulation of the primary break-up of a liquid jet, International Journal of Multiphase Flow 33 (2007) 510 – 524.

[64] J. Hernández, J. López, P. Gómez, C. Zanzi, F. Faura, A new volume of fluid method in three dimensionspart i: Multidimensional advection method with face-matched flux polyhedra, International Journal for Numerical Methods in Fluids 58 (2008) 897–921.

[65] S. Koshizuka, Y. Oka, Moving-particle semi-implicit method for fragmentation of incompressible fluid, Nuclear Science and Engineering 123 (1996) 421–434.

[66] C. E. Kees, I. Akkerman, M. W. Farthing, Y. Bazilevs, A conservative level set method suitable for variable-order approximations and unstructured meshes, J. Comput. Phys. 230 (2011) 4536–4558.

[67] A. Jarauta, P. Ryzhakov, J. Pons-Prats, M. Secanell, An implicit surface tension model for the analysis of droplet dynamics, Journal of Computational Physics 374 (2018) 1196–1218.

[68] D. Gerlach, G. Tomar, G. Biswas, F. Durst, Comparison of volume-of-fluid methods for surface tension-dominant two-phase flows, International Journal of Heat and Mass Transfer 49 (2006) 740–754.

[69] S.-R. Hysing, S. Turek, D. Kuzmin, N. Parolini, E. Burman, S. Ganesan, L. Tobiska, Quantitative benchmark computations of two-dimensional bubble dynamics, International Journal for Numerical Methods in Fluids 60 (2009) 1259–1288.

[70] S. Hysing, Mixed element fem level set method for numerical simulation of immiscible fluids, Journal of Computational Physics 231 (2012) 2449–2465.